



## UvA-DARE (Digital Academic Repository)

### Trigger of the ubiquitous surface band bending in 3D topological insulators

Frantzeskakis, E.; Ramankutty, S.V.; de Jong, N.; Huang, Y.K.; Pan, Y.; Tytarenko, A.; Radovic, M.; Plumb, N.C.; Shi, M.; Varykhalov, A.; de Visser, A.; van Heumen, E.; Golden, M.S.

**DOI**

[10.1103/PhysRevX.7.041041](https://doi.org/10.1103/PhysRevX.7.041041)

**Publication date**

2017

**Document Version**

Final published version

**Published in**

Physical Review X

**License**

CC BY

[Link to publication](#)

**Citation for published version (APA):**

Frantzeskakis, E., Ramankutty, S. V., de Jong, N., Huang, Y. K., Pan, Y., Tytarenko, A., Radovic, M., Plumb, N. C., Shi, M., Varykhalov, A., de Visser, A., van Heumen, E., & Golden, M. S. (2017). Trigger of the ubiquitous surface band bending in 3D topological insulators. *Physical Review X*, 7(4), Article 041041. <https://doi.org/10.1103/PhysRevX.7.041041>

**General rights**

It is not permitted to download or to forward/distribute the text or part of it without the consent of the author(s) and/or copyright holder(s), other than for strictly personal, individual use, unless the work is under an open content license (like Creative Commons).

**Disclaimer/Complaints regulations**

If you believe that digital publication of certain material infringes any of your rights or (privacy) interests, please let the Library know, stating your reasons. In case of a legitimate complaint, the Library will make the material inaccessible and/or remove it from the website. Please Ask the Library: <https://uba.uva.nl/en/contact>, or a letter to: Library of the University of Amsterdam, Secretariat, Singel 425, 1012 WP Amsterdam, The Netherlands. You will be contacted as soon as possible.

*UvA-DARE is a service provided by the library of the University of Amsterdam (<https://dare.uva.nl>)*

# Trigger of the Ubiquitous Surface Band Bending in 3D Topological Insulators

E. Frantzeskakis,<sup>1,2,\*</sup> S. V. Ramankutty,<sup>1</sup> N. de Jong,<sup>1</sup> Y. K. Huang,<sup>1</sup> Y. Pan,<sup>1</sup> A. Tytarenko,<sup>1</sup> M. Radovic,<sup>3</sup> N. C. Plumb,<sup>3</sup> M. Shi,<sup>3</sup> A. Varykhalov,<sup>4</sup> A. de Visser,<sup>1</sup> E. van Heumen,<sup>1</sup> and M. S. Golden<sup>1,†</sup>

<sup>1</sup>*Van der Waals-Zeeman Institute, Institute of Physics (IoP), University of Amsterdam, Science Park 904, 1098 XH, Amsterdam, Netherlands*

<sup>2</sup>*CSNSM, Université Paris-Sud, CNRS/IN2P3, Université Paris-Saclay, 91405 Orsay cedex, France*

<sup>3</sup>*Swiss Light Source, Paul Scherrer Institut, CH-5232 Villigen, Switzerland*

<sup>4</sup>*Helmholtz-Zentrum Berlin für Materialien und Energie, Elektronenspeicherring BESSY II, Albert-Einstein-Strasse 15, 12489 Berlin, Germany*

(Received 10 July 2017; revised manuscript received 25 September 2017; published 20 November 2017)

The main scientific activity in the field of topological insulators (TIs) consists of determining their electronic structure by means of magnetotransport and electron spectroscopy with a view to devices based on topological transport. There is, however, a caveat in this approach. There are systematic experimental discrepancies on the electronic structure of the most pristine surfaces of TI single crystals as determined by Shubnikov–de Haas oscillations and by angle-resolved photoelectron spectroscopy (ARPES). We identify intense ultraviolet illumination—that is inherent to an ARPES experiment—as the source for these experimental differences. We explicitly show that illumination is the key parameter, or in other words, the trigger, for energetic shifts of electronic bands near the surface of a TI crystal. This finding revisits the common belief that surface decoration is the principal cause of surface band bending and explains why band bending is not a prime issue in illumination-free magnetotransport studies. Our study further clarifies the role of illumination on the electronic band structure of TIs by revealing its dual effect: downward band bending on very small time scales followed by band flattening at large time scales. Our results therefore allow us to present and predict the complete evolution of the band structure of TIs in a typical ARPES experiment. By virtue of our findings, we pinpoint two alternatives of how to approach flat-band conditions by means of photon-based techniques and we suggest a microscopic mechanism that can explain the underlying phenomena.

DOI: [10.1103/PhysRevX.7.041041](https://doi.org/10.1103/PhysRevX.7.041041)

Subject Areas: Condensed Matter Physics,  
Topological Insulators

## I. INTRODUCTION

New states of matter in which broken symmetry, topology, and spin play a central role can lead to emerging applications in the fields of spintronics and quantum computation. Prime examples of relevant materials platforms in which to realize such novel fermionic degrees of freedom include topological insulators [1–8], topological crystalline insulators [9–12], and the recently discovered Weyl semimetals [13–15]. Among these compounds, Bi-based 3D topological insulators (TIs) have attracted enormous scientific interest due to their simple electronic band structure at the Fermi level comprising a single, surface-localized state with linear energy-momentum dispersion [3–6,16]. This so-called Dirac cone harbors spin-polarized

electronic states that cross at a special, symmetry-protected spin-degenerate point, known as the Dirac point.

The energy of the Dirac point ( $E_D$ ) and its tunability are crucial factors as regimes of topological or trivial transport can be obtained, depending on whether—or not—other electronic states are crossing the Fermi level. Moreover, the possibility of tuning  $E_D$  in the bulk energy gap, in combination with the large Fermi wavelength for the Dirac fermions, paves the way towards topological superconductors and new fundamental excitations known as Majorana zero modes [17–19]. Tunability of the Dirac energy with respect to the Fermi energy ( $E_F$ ) has been previously demonstrated in Bi-based TIs via controlled surface decoration [8,20–29], changes in bulk stoichiometry [27,30–36], and exposure to intense UV illumination [37–39].

Most of the experimental results on the electronic band structure of TIs come from the direct view of the energy-momentum dispersion provided by angle-resolved photoelectron spectroscopy (ARPES) [3,4,7,8,16,21–24,26–28,32–35,37,39–48] or from an extraction of the Fermi surface size using the frequency of quantum oscillations (QOs) observed in magnetotransport experiments

\*emmanouil.frantzeskakis@csnsm.in2p3.fr

†m.s.golden@uva.nl

*Published by the American Physical Society under the terms of the Creative Commons Attribution 4.0 International license. Further distribution of this work must maintain attribution to the author(s) and the published article's title, journal citation, and DOI.*

[31,36,41,47–61]. Although both experimental techniques are very accurate in determining the details of the electronic band structure of TIs (for QOs only for  $E = E_F$ ), there is a systematic mismatch in the acquired results. Namely, ARPES results tend to place the Dirac point  $E_D$  farther below the Fermi level than QO data from the same compounds. In the case of the surface states of 3D TIs, there cannot be a surface versus bulk discrepancy, as, when executed well on sufficiently bulk-insulating samples, the QO data are also from the surface of the sample. The upshot is that the ARPES experiments appear more sensitive to band bending effects induced by unwanted surface decoration from residual gas atoms. This is something of a mystery, since ARPES measurements take place in ultra-high vacuum (UHV) conditions, i.e., under a pressure that is several orders of magnitude lower than that typically found in magnetotransport experiments. Most importantly, the mismatch in the results between spectroscopy and QOs raises serious questions as to whether the results and conclusions obtained by the dominating spectroscopic probe of topological surface states, namely ARPES, can be safely ported to the world of transport-based devices based on topological insulators.

In this paper, we discuss the discrepancies between the two experimental techniques and we present new ARPES data that reveal the drivers behind them. This allows the proposition of an ARPES protocol that enables trustworthy extraction of  $E_D$  values that are relevant to those obtained in transport studies. In order to reach this goal, we track the complete evolution of the band structure in several different TI compounds during a typical ARPES experiment. In contrast to the common belief that surface decoration is solely responsible for the initial downward band bending, we reveal that the real trigger is illumination. These results point to a simple mechanism that can explain the complex evolution of the electronic band structure of TIs at different time scales during exposure to intense EUV illumination. The proposed mechanism boils down to the interplay of fundamental microscopic processes such as molecular adsorption, photodissociation (photolysis), photoionization, photostimulated desorption, and surface photovoltage.

## II. RESULTS

We start by discussing the systematic discrepancy between results on comparable TI single crystals obtained by means of ARPES and transport experiments. The radial scatter plot of Fig. 1 compares the binding energy of the Dirac point obtained either by ARPES experiments (red circles) or by Shubnikov–de Haas (SdH) oscillations in magnetotransport (blue circles). The value of  $E_F - E_D$  (i.e., the Dirac point binding energy) increases radially: the border of the inner circle corresponds to zero binding energy of the Dirac point (i.e.,  $E_D = E_F$ ) and each tick denotes an increase of 100 meV. Each data point in the figure corresponds to a different experimental study in the

literature, showing the work of many groups, including our own, and results are shown for five different TI compounds. A general conclusion can be readily made. ARPES shows a systematically higher binding energy for the Dirac point than magnetotransport experiments. We note that several ARPES studies [7,8,20–24,26,28,29,32,39,43,45] have observed energy shifts to higher binding energies because of surface band bending on intentional and unintentional (“aging”) surface decoration. In order to maintain a fair comparison with magnetotransport, the filled red circles in Fig. 1 correspond to surfaces that have been neither decorated nor aged in UHV. Such data points have been acquired in a time frame between a few minutes and 2 h after cleavage. Empty markers show the value of  $E_D$ —by means of ARPES—on exposure to air (empty squares) or on increasing exposure to the residual UHV gases (empty circles). Such surface decoration might be an even more important issue in magnetotransport experiments, as such experiments do not take place in a UHV environment and generally do not involve *in situ* cleavage of the single crystalline sample. However, the magnetotransport data seem relatively insensitive to surface decoration, as the binding energies of the Dirac point are smaller than even the most pristine surfaces studied by ARPES.

Figure 1 makes it clear that surface decoration alone cannot be the key to the observed differences between ARPES and QO experiments, and thus the conclusion drawn earlier—that the  $E_D$  values obtained by SdH oscillations cannot be systematically reproduced by ARPES even in the most pristine surfaces—is still valid. In the following, we explain where the difference in the experimentally determined  $E_D$  comes from between the two techniques, and we discuss whether we can approach the SdH values by means of ARPES.

Figure 2 shows the first experimental evidence that the surface band bending of 3D TIs is modified substantially on exposure to EUV illumination of a duration of a single second, compared to the typical time scale of ARPES data collection for an  $I(E, k)$  image of tens of seconds or even several minutes. In order to highlight that the development of the band bending is indeed dominated by EUV exposure, and not by simple surface decoration with residual UHV gases, as has generally been believed [7,8,20–24,43], we construct the following experimental protocol. Firstly, we intentionally expose all cleavage surfaces to residual UHV gases for 3 h at low temperature before the first measurement. Secondly, we limit the duration of each measurement (and hence the EUV exposure) to a minimum of 1–2 s using a photon flux of  $3.2 \times 10^{21}$  photons/(s m<sup>2</sup>). The optimization of the sample position with respect to the electron energy analyzer and the photon beam, and the adjustment of the emission angles—such that the detector image cuts through the center of the Brillouin zone—are carried out on a part of the cleave 1 or more millimeters away from the point where the data of Figs. 2 and 3 are recorded. This

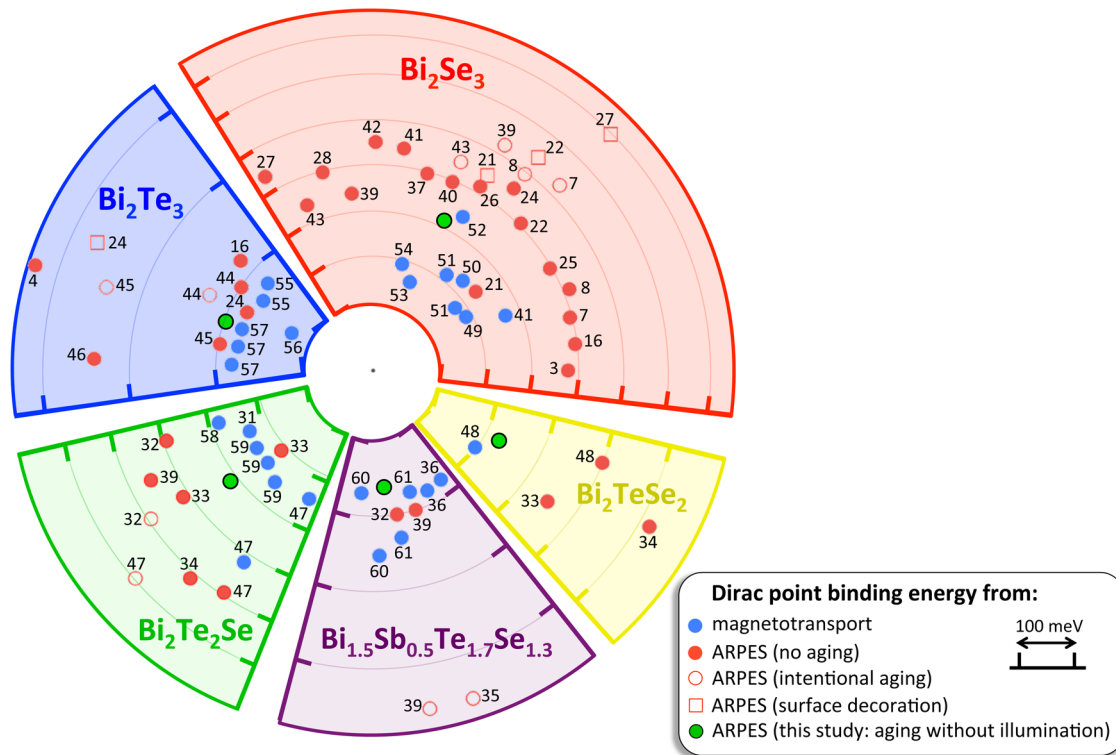


FIG. 1. Discrepancies between the experimentally determined Dirac point energies for TI surface states between ARPES and quantum oscillations. The graphic shows the binding energy of the Dirac point ( $E_D$ ) in five different 3D topological insulator materials as extracted from published transport (blue symbols) and ARPES (red symbols) studies. The border of the inner circle corresponds to zero binding energy of the Dirac point (i.e.,  $E_D = E_F$ ). The binding energy increases radially with each tick denoting an increase of 100 meV. Notice the different axes scale for each compound. Filled circles denote data from samples which have not been intentionally aged in UHV, and measurements have been typically performed within an hour of sample cleavage. Empty squares and circles denote that air exposure and intentional aging under UHV conditions have been carried out, respectively. Green circles show the value of  $E_D$  extracted from ARPES data presented in this study: these surfaces have been intentionally exposed to UHV residual gases for 3 h, but their total exposure to external illumination was of only a single second. The green data points are taken from the ARPES data presented in Figs. 2 and 3 for each compound, whereby we note a slight variation in the composition of the  $\text{Bi}_{2-x}\text{Sb}_x\text{Te}_{3-y}\text{Se}_y$  used (i.e.,  $x = 0.54$  instead of 0.5), and that the green ARPES data point in the  $\text{Bi}_2\text{TeSe}_2$  panel is from the related system  $\text{BiSbTeSe}_2$ . The number next to each red and blue marker is the literature reference from which  $E_D$  is extracted.

means that the  $E_D$  values for the locations measured for Figs. 2 and 3 represent those for regions with carefully controlled EUV exposure [62].

Inspection of the green symbols in Fig. 1—showing  $E_D$  for EUV exposures of only 1–2 s—reveals that the Fermi energy is much closer to the Dirac point for each of the TI materials, compared to the red, open circles in Fig. 1 from other decorated surfaces which have not been intentionally “kept in the dark” [7,8,32,39,43,47]. This simply means that in the determination of  $E_D$  using ARPES, every second counts.

We capture the rapid evolution of the surface band structure shown in the right-hand panel of Fig. 2 by keeping the sample in the dark, except for successive, 1–2 s short  $I(E, k)$  ARPES exposures on the same spatial location. The effect of EUV exposure is striking: the surface band structure changes within the very first seconds. At the photon flux used, as little as 40 s EUV exposure yields the  $I(E, k)$  images shown in the center column of Fig. 2, and

analysis of these data shows that  $E_D$  is already approaching values typical for decorated surfaces. As a matter of fact, in terms of increasing the energy separation between  $E_D$  and  $E_F$ , a few seconds of bright EUV light impacts the surface band structure of TI single crystals more than does an exposure to residual UHV gases in the dark in excess of a couple of hours.

Aided by this new insight, we can assess the implications of these results for previous ARPES studies. Even exploiting the high EUV photon flux of a third-generation synchrotron source, the typical acquisition time for an  $I(E, k)$  image with a reasonable signal-to-noise ratio is of the order of 1–2 min. Moreover, the first measurement is usually preceded by the optimization of the spatial and angular positions of the sample, a process that usually takes place in the same sample location and the main measurements themselves. This means that for the great majority of the published ARPES data, the sample surface has been exposed to EUV light for at least a few minutes before the

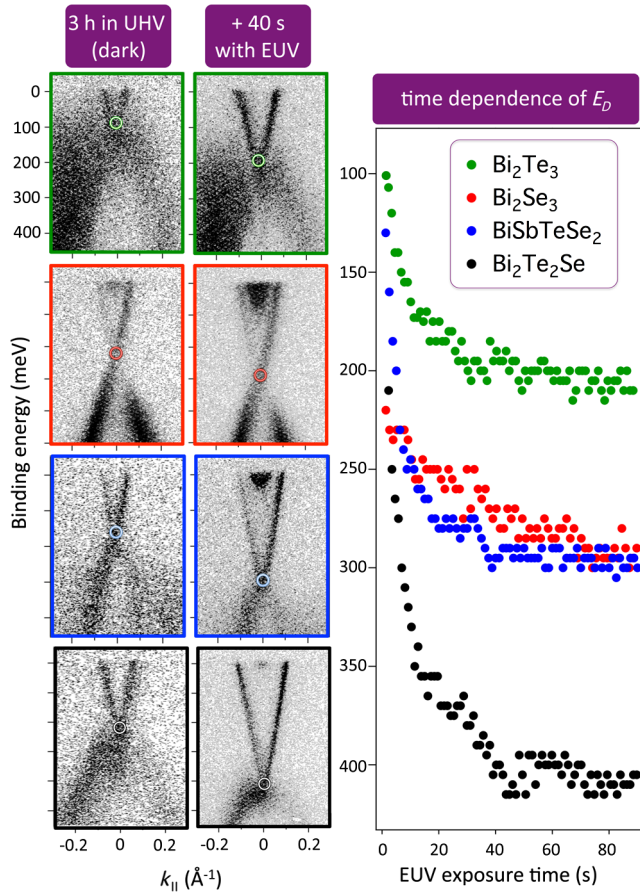


FIG. 2. The striking effect of illumination on the evolution of band bending during a typical ARPES experiment on TIs. Left-hand (center) columns of  $I(E, k)$  images: Surface band structure of four different TI compounds recorded using an EUV exposure of only 1 s (40 s), after the cleavage surface had been exposed to residual UHV gases for 3 h. Right-hand column: Very rapid evolution of  $E_D$  from the first moment of EUV illumination, whereby the left-hand  $I(E, k)$  images underlie the first (second for  $\text{BiSbTeSe}_2$ ) data point of each curve in the right-hand panel. The pressure before and during the ARPES measurements was  $1.0 \times 10^{-10}$  and  $5.0 \times 10^{-11}$  mbar, respectively. All data have been acquired at 16 K using a photon flux of  $3.2 \times 10^{21}$  photons/( $\text{s m}^2$ ). The photon energy was 30 eV for  $\text{Bi}_2\text{Se}_3$  and 27 eV for all the other compounds.

acquisition of the first  $I(E, k)$  band structure image at a specific location. Given the speed of the EUV-triggered downward band bending on decorated (or aged) surfaces taking place within the first seconds of exposure, it is certainly feasible that this whole process can go unnoticed. There is therefore no surprise that changes in the electronic band structure have been solely ascribed to the adsorbed gases and no reference is usually made to the role of the radiation that is part of an ARPES experiment.

Returning to the discrepancy between ARPES and QO data on the size of the Fermi surfaces of the Dirac cone (and hence the energy difference between  $E_D$  and  $E_F$ ), it is clear that the huge effect of EUV light exposure lies at the core of

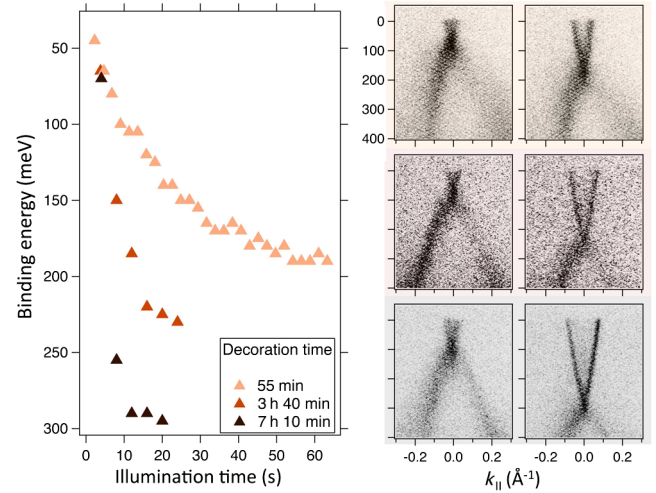


FIG. 3. The effect of surface decoration on the evolution of surface band bending during a typical ARPES experiment on 3D TIs. Left-hand column: Binding energy of the Dirac point in  $\text{Bi}_{1.46}\text{Sb}_{0.54}\text{Te}_{1.7}\text{Se}_{1.3}$  as a function of illumination time after the surface has been exposed for differing times to UHV residual gas molecules, as given in the legend. Center (right-hand) panels:  $I(E, k)$  images showing the surface band structure of  $\text{Bi}_{1.46}\text{Sb}_{0.54}\text{Te}_{1.7}\text{Se}_{1.3}$  which underlie the data points in the left-hand graphic for EUV exposure times of 1 s (20 s). The pressure before and during measurements was  $1.0 \times 10^{-10}$  and  $5.0 \times 10^{-11}$  mbar, respectively. All data have been acquired at 16 K using a photon flux of  $3.2 \times 10^{21}$  photons/( $\text{s m}^2$ ), with a photon energy of 27 eV.

the reported disagreement. Essentially, with the first few seconds of EUV exposure required to perform an ARPES measurement, the Dirac point shifts downward by more than 0.1 eV. Thus, due to its nature as an ionizing technique, ARPES sees a band-bent version of the band structure, different from that extracted from quantum oscillations in magnetotransport experiments. Logically, the longer the exposure to EUV radiation before the acquisition of the ARPES data measurement, the larger the discrepancy between the two techniques, although the fact that a significant shift already takes place within the first half a minute should not be overlooked.

From the data and discussion thus far, it is incontrovertible that EUV triggering is a vital part of the band bending process. However, further questions may naturally arise such as, (i) is the amount of surface decoration of importance in determining the evolution of the band bending and (ii) can we extrapolate the ARPES results presented in Fig. 2 to  $t = 0$  in order to obtain  $E_D$  under flat-band conditions?

We can answer the first question positively and the second question negatively using the data presented in Fig. 3. The left-hand panel of the figure tracks the evolution of  $E_D$  in three  $\text{Bi}_{1.46}\text{Sb}_{0.54}\text{Te}_{1.7}\text{Se}_{1.3}$  (BSTS1.46) samples that have been measured using the same photon flux, but whose cleavage surfaces are held in residual UHV gases for

differing time periods before the first EUV exposure that is inevitably coupled to the ARPES acquisition process. The differences between the time dependence of  $E_D$  in the three cases are marginal at the outset, and for short illumination times the  $I(E, k)$  images look rather similar (see center column of Fig. 3). However, as the ARPES experiments and the ensuing EUV exposure progress, the sample with the longest *a priori* exposure to residual gases, and presumably the largest number of adatoms on its cleavage surface, exhibits a significantly more rapid evolution of its downward band bending. Thus, already at time scales as short as 20 s total EUV exposure (right-hand column of Fig. 3), the three band structure images start to look quite different. This argues that the amount of surface decoration does still play a significant role, bearing great influence on both the saturation point and the evolution speed of the downward band bending. This said, the crucial role in the EUV light exposure in triggering the downward band bending should not be forgotten. Consequently, it is evident that we cannot simply extrapolate the curves of either Fig. 2 (3 h of UHV residual gas) or Fig. 3 (~1, ~4, and 7 h of UHV residual gas) to  $t = 0$ , in an attempt to extract the energy difference between  $E_F$  and  $E_D$  under flat-band conditions, as such a procedure would ignore the differences in the

UHV “decoration time” from when the cleavage surface was in the dark prior to the first illumination. Nevertheless, what Figs. 2 and 3 show is that as long as the ARPES acquisition time is kept very rapid—meaning well below 5 s—the very first ARPES measurement can provide us with an upper limit of the energy separation of  $E_F$  and  $E_D$  for flat-band conditions. We note that the Fermi level (flat-band conditions) should be pinned close to the conduction band minimum and the valence band maximum (VBM) for *n*-type and *p*-type samples, respectively [63]. Past studies have identified *n*-type carriers in  $\text{Bi}_2\text{Se}_3$  and  $\text{Bi}_2\text{Te}_2\text{Se}$  [31,39,42,47,58,59,64,65] and *p*-type carriers in  $\text{Bi}_2\text{Te}_3$ ,  $\text{BiSbTeSe}_2$ , and other compounds of the  $\text{Bi}_{2-x}\text{Sb}_x\text{Te}_{3-y}\text{Se}_y$  family [39,57,64,65]. The initial  $I(E, k)$  images—recorded within 5 s of the onset of illumination—for the five TI compounds whose data are shown in Figs. 2 and 3 are in good agreement with these previous assignments, with the VBM of the *p*-type compounds lying between 50–130 meV below the Fermi level, while its binding energy exceeds 200 meV for all of the *n*-type compounds.

Figure 3 illustrates that the speed of development of the downward band bending increases as the degree of surface decoration prior to illumination increases. Figure 4 shows that this degree of decoration is not the only parameter, and

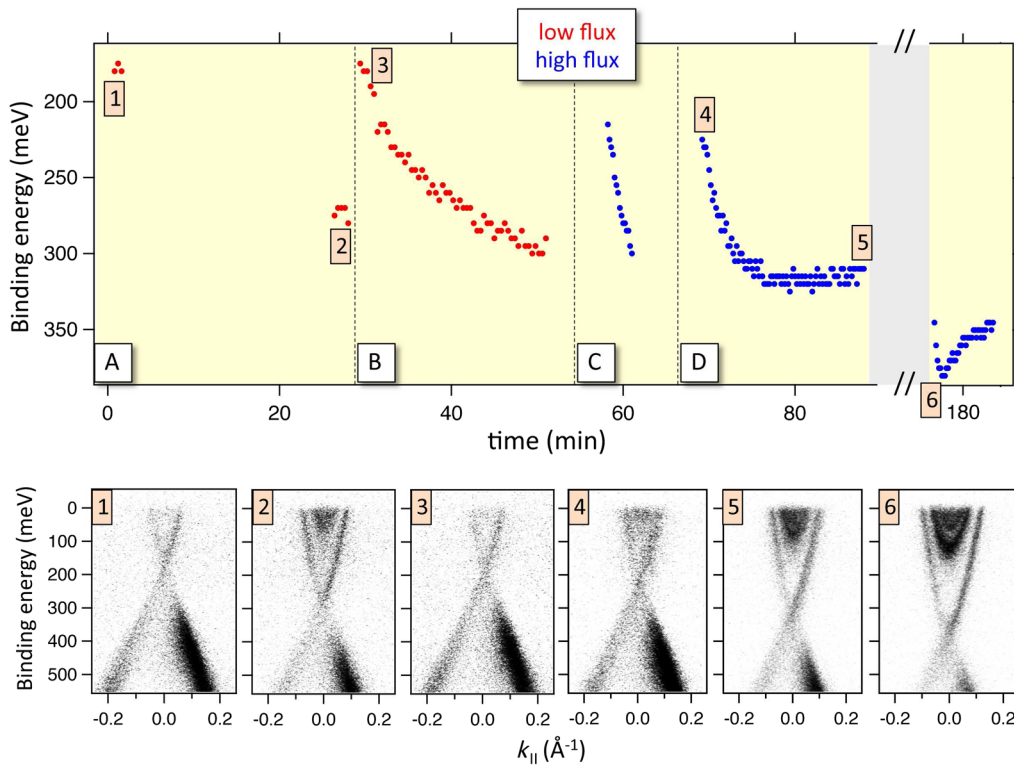


FIG. 4. The local character of EUV-induced surface band structure changes in 3D TIs, and the effect of photon flux. The upper panels show the evolution of  $E_D$  in  $\text{Bi}_2\text{Se}_3$  on exposure of four different sample locations labeled A–D to low (red) and high (blue) photon flux. Vertical dashed lines denote the change of sample location. The lower panels show the  $I(E, k)$  images corresponding to the numbered points (1–6) superimposed on the curves in the uppermost panels. The pressure during measurements was  $1.5 \times 10^{-10}$  mbar. The flux corresponding to the red data points was 3–4 times lower than the flux corresponding to the blue data points. All data have been acquired at 38 K using a photon energy of 30 eV.

that variations of the photon flux from one experiment to the next can also accelerate or decelerate the evolution of the downward band bending. The upper panels of Fig. 4 track the Dirac point energy over time in a sample of  $\text{Bi}_2\text{Se}_3$  which, in differing locations, has been exposed to both low (red data points, panels A and B) and high photon fluxes (blue data points, panels C and D). The reduced photon flux is obtained by detuning the undulator gap with respect to the ideal value for the photon energy being selected by the monochromator, and from the ARPES signal intensity, we conclude that the attenuation is by a factor of 3–4. At the beam line and end station combination used for the experiments underlying Fig. 4, acquisition as fast as that used for Figs. 2 and 3 would have yielded insufficient signal-to-noise ratio, and thus the focus is placed on the behavior over the longer time scales of minutes, rather than seconds. Experiments are performed at four different sample locations (labeled A, B, C, and D in Fig. 4), each sufficiently well separated from the others so that each location enables an independent experiment. One can readily see that the downward time evolution of  $E_D$  is more rapid when the photon flux is higher (blue data points in panels C and D). Turning to the lower panels of Fig. 4, which show  $I(E, k)$  images recorded along the timer or location series as shown in the upper panels of the figure, a comparison of the  $I(E, k)$  images 1, 2, and 3 shows that the surface band structure changes are essentially local in nature, as  $E_D$  goes back to close to its initial value when a previously unirradiated sample location is measured. For the start of the high-flux acquisition series shown in panel 4 of Fig. 4, we see that  $E_D$  is at slightly higher binding energy than the other “fresh” scans (1 and 3). We ascribe this difference to a combination of the very fast initial evolution of the surface band structure under high-flux illumination that cannot be captured in this case and a slow but finite spreading out of local surface band structure changes away from the illuminated location. The local character of photoinduced surface band structure changes has been discussed in detail in Ref. [62], and this was used to write micrometric structures in which topologically trivial electronic states could be pushed above the Fermi level in predefined areas.

After the downward band bending affecting the surface band structure in location D had saturated (panel 5 of Fig. 4), the EUV exposure was halted for 90 min, while leaving the sample at the measurement position (see the gray area in the right-hand top panel of the figure). On subsequent continuation of the EUV exposure, the downward band bending is seen to grow rapidly once again, thereby shifting  $E_D$  to an even higher value of binding energy, as shown in panel 6. Finally, as the exposure of the sample to high-flux radiation continues,  $E_D$  starts shifting back to lower values, in a manner first presented and described in detail elsewhere [62].

Taking the data presented in Figs. 1–4 together, we show that there is a persistent discrepancy between the Dirac

point energies extracted from published ARPES data and those from Fermi surface analyses based on quantum oscillation experiments. We show that the EUV exposure inherent to the ARPES experiment itself triggers the downward band bending, and that this lies at the root of the discrepancy with the transport data. We also show that both the initial surface decoration with adatoms from the UHV residual gases and the photon flux used to carry out the photoemission experiment are parameters that influence the speed with which the downward band bending evolves in common Bi-based 3D TI compounds. ARPES is a central experimental technique in the TI field, but the data indicate significant changes in the energy separation between the Fermi and Dirac energies on the time scale of mere seconds after the very first exposure to EUV light. Therefore, in the following section we show the results of experiments designed to reveal the complete evolution of the surface band structure for a representative 3D topological insulator during a standard ARPES experiment at a large-scale facility, covering both the downward band bending and subsequent upward shift of the bands. We discuss a simplified mechanism that can explain these changes.

### III. DISCUSSION

It is clear by now that determining the energy of the Dirac point in topological insulators by means of a photon-based experimental technique like ARPES is far from trivial. If the samples enable sufficient suppression of the bulk conductivity, transport studies possess a clear advantage: even though the surface is certainly exposed to external gas molecules, these do not affect its surface electronic band structure because the trigger for downward band bending active in ARPES—the strong EUV illumination—is missing. On the other hand, ARPES is very sensitive to the surface states, and provides a direct access to the  $E$  versus  $k$  dispersion relation, something which is of great value. Thus, despite the complications brought with the EUV illumination “built into” ARPES, it is important to complete the discussion on how to understand the results expected in a standard, low-temperature ARPES experiment on 3D TI surface states. In the following paragraphs, we focus on the mechanism behind the time-dependent evolution of the band structure, and suggest two alternative routes that allow flat-band conditions to be approached and hence the “real” energy value of the Dirac point to be determined using ARPES.

Our results establish that the evolution of the surface band structure of common Bi-based TIs during an ARPES experiment—and more generally under any experiment involving intense (E)UV illumination—is not random. It is determined by the initial surface decoration (as shown in Fig. 3) and the magnitude of the photon flux (as shown in Fig. 4). However, the whole band bending process is triggered only by the onset of the EUV illumination itself

(as shown in Fig. 2). The interplay between these parameters results in a characteristic time-dependent behavior of  $E_D$ , an example of which is shown in the upper panel of Fig. 5. Parts of this time-dependent process have certainly been discussed in the framework of the earlier figures in this paper and in a number of prior publications [7,8,21–23,38,39], yet the data of Fig. 5 present the first comprehensive description of the complete temporal evolution spanning from the very first seconds to several hours of continuous EUV illumination on the same sample location.

The data points in the upper panel of Fig. 5 are actually from a cleaved crystal of the bulk-insulating 3D TI BiSbTeSe<sub>2</sub> which has been exposed to residual UHV gases for 3 h before starting illumination. The logarithmic time scale chosen for the  $x$  axis of Fig. 5 stresses the importance of the first seconds of light exposure. The  $I(E, k)$  image insets illustrate the surface band structure. At first (leftmost

image), the Fermi level lies 130 meV above the Dirac point, and no bulk conduction band states are seen below the Fermi level. As time progresses,  $E_D$  continuously increases, saturating at 300 meV below the Fermi energy (center inset image). With the photon flux used for these data of  $3.2 \times 10^{21}$  photons/(s m<sup>2</sup>), this saturation is achieved in less than 5 min, and within this time scale, the bulk conduction band has been shifted into the occupied part of the energy spectrum. On further EUV exposure, the trend is inverted, whereby  $E_D$  then starts to shift back towards  $E_F$ , within 3–4 hours reaching an energy value that is comparable to that after the first second of illumination (rightmost inset). The observed spectral broadening and the trace of a conduction band tail are the result of the inhomogeneous intensity profile of the beam spot, and this phenomenon has been the focus of previous investigations [39,62]. Here, we stress the opposite trends of the two photoinduced phenomena at small and large time

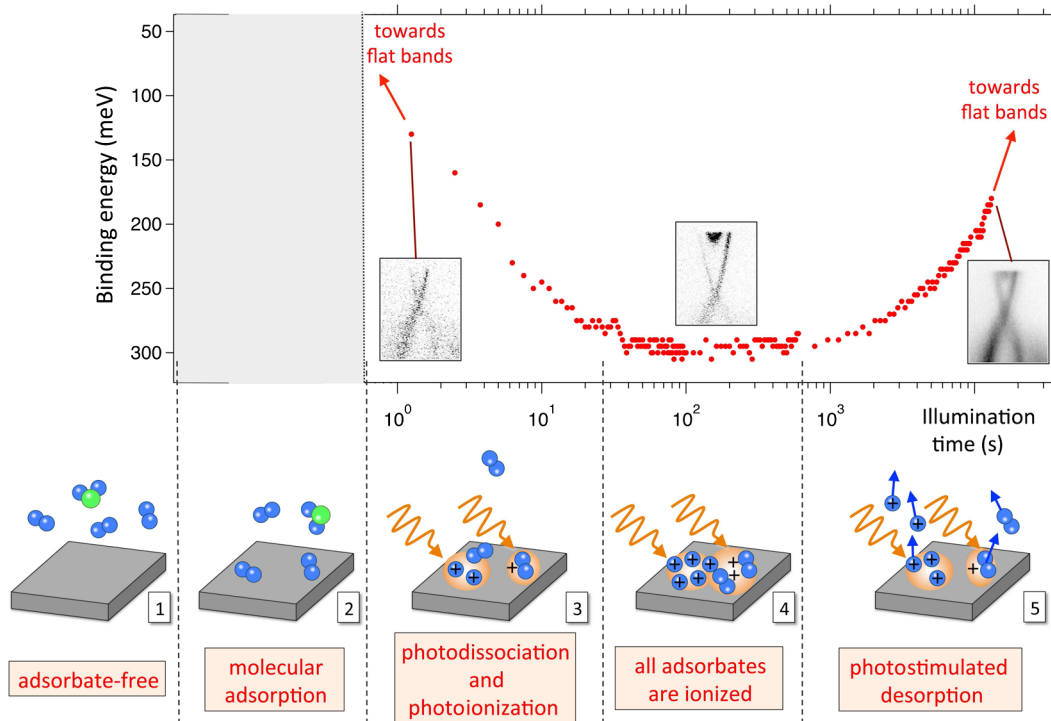


FIG. 5. The complete evolution of the band structure of TIs under intense illumination and a schematic of the underlying mechanism. Top: Evolution of  $E_D$  at different time scales obtained on a single surface location of BiSbTeSe<sub>2</sub> during a standard ARPES experiment. From left to right: Intense illumination promotes downward band bending until a saturation point and from then on further exposure tends to flatten the bands again. Red arrows indicate that true flat-band conditions in an ARPES experiment on these materials can only be achieved at very short or very long time scales. The insets in the upper panel show the corresponding  $I(E, k)$  diagrams at different illumination times. Prior to illuminating the surface location that was finally studied with ARPES, the sample had been exposed to residual gas molecules for 3 h, represented by the gray shaded area in the upper panel. The base pressure before and during measurements was, respectively,  $1.0 \times 10^{-10}$  and  $5.0 \times 10^{-11}$  mbar. All data have been acquired at 16 K using a 27 eV photon flux of  $3.2 \times 10^{21}$  photons/(s m<sup>2</sup>). Bottom: Schematics of the five steps underlying our observations. Vertical dashed lines denote the time period to which each step corresponds. Step 1: immediately after cleavage, the sample surface is free of adsorbates. Step 2: residual gas molecules adsorb on the sample surface during the period while the latter is held in the “dark.” Step 3: under the influence of the intense EUV photon beam required to do ARPES, adsorbed molecules start to dissociate into single adatoms in the illuminated sample location [38]. Step 4: all adsorbed molecules are dissociated and/or photoionized, and band bending reaches a maximum. Step 5: Photostimulated desorption of adatoms and surface photovoltage (not illustrated) come into play and the bands shift back up again.

scales, as well as the remarkable symmetry of the logarithmic time-dependent curve around the saturation point.

Thus, we are now in a position to give a complete answer to the question of how we can approach flat-band conditions in an ARPES experiment on such topological insulators. For a photon flux of  $3.2 \times 10^{21}$  photons/(s m<sup>2</sup>), which is of the order of the standard photon flux at a third-generation synchrotron facility, downward band bending is reduced to a minimum at illumination times either smaller than 1 s or exceeding 4–5 hours. We have previously shown that approaching flat-band conditions at large time scales is only possible at high photon fluxes and energies [39], and that the data are always subject to spectral broadening [39,62]. Therefore, very short illumination times represent the preferred option to approach flat-band conditions. We note that by reducing the flux, the initial, downward band bending can be decelerated, so as to fit such a “fast” measurement into the practical time window of a given ARPES setup, thus yielding band structures that are even closer to flat bands (see Fig. 4). ARPES experiments at very small or very large time scales are hence a prerequisite for meaningful comparison with the results from transport. Indeed, the ARPES data points from the very first illumination on each sample in this paper (shown as green markers in Fig. 1) are in reasonable agreement with the SdH data.

We can now turn to the origin of the observed time dependence of the electronic band structure. Cartoons in the bottom row of Fig. 5 illustrate a sequence of microscopic processes underlying each experimental step. Right after cleavage, the surface is pristine and there is no band bending (panel 1). While it ages in the dark, the cleavage surface is decorated with residual gas molecules (panel 2). Specifically, molecular hydrogen—as the dominant residual gas in clean UHV vacuum systems—is a possible adsorbate. It has been proposed to photodissociate, resulting in stronger bonding with the sample surface and donation of electron density to the TI [38]. Also conceivable is the photoionization of adsorbed molecules. Both processes (photodissociation and photoionization) result in a positive ion layer developing at the surface-vacuum interface, resulting in downward band bending [7,8,21–23,38] (panel 3). When all adsorbed molecules in the illuminated area either have dissociated (in the case of H<sub>2</sub>) or in any case have become ionized, the binding energy of the Dirac point and the downward band bending reach a maximum (panel 4). Nevertheless, the role of illumination is not limited to dissociation or ionization of molecular species: irradiation may also promote the desorption of adatoms and molecules. Photostimulated desorption plays a role in the observed flattening of the bands with  $E_D$  moving back to lower binding energies seen in panel 5. In addition, an additional photoinduced electronic phenomenon, known as the surface photovoltage (SPV) effect, creates electron-hole pairs in the space-charge region that act in synergy

with photostimulated desorption to further decrease the downward band bending [39].

The mechanism based on the combination of molecular adsorption, photodissociation, ionization, photostimulated desorption, and SPV can explain our observations and the results of previous studies [7,8,21–23,38,43]. In a typical ARPES experiment, the photon beam does not stay on the same sample location long enough to observe the relatively slow upward shift of  $E_D$  seen in the right-hand side of Fig. 5. Most of the past literature has been therefore focused on the development of the initial downward band bending that is governed by molecular adsorption, photodissociation, and/or ionization. The latter two processes are relatively fast, and thus can remain unnoticed as the overall dynamics would then be governed by the slow molecular adsorption step. By intentionally increasing the time of exposure to residual gas atoms before the beginning of irradiation, we separate photodissociation and ionization from molecular adsorption. While adsorption increases during aging in the dark, there are no photons to generate the charged surface layer. Thus, immediately upon the onset of illumination, the effects of photodissociation or ionization become clear. Our strategy to experimentally separate the two processes and to decrease the time window of the measurements themselves so as to better match the more rapid dynamics of photodissociation and ionization reveals that illumination is the essential trigger of the time-dependent band structure changes in Bi-based TIs. This result adds important nuance to the common belief that adsorption is the sole process at the origin of band bending.

Can this new insight be tested? Returning to Fig. 4, the time-dependent curve shown at location D in the upper panel can now be reexamined. On saturation of the downward band bending (point 5 and panel 5), a steady state is reached between dissociation and ionization of adsorbed molecules on one hand, and photostimulated desorption and SPV on the other hand. While the sample is then kept further in the dark, the latter effects are “turned off” and molecular adsorption continues. Upon resuming irradiation, photodissociation and ionization of the newly adsorbed molecules comes back into play, governing the first seconds of illumination and leading to a renewed increase in the downward band bending. At later times, the upturn in the Dirac point energy suggests that photostimulated desorption is important in reasserting the flattening of the bands. Summarizing this discussion, the band structure dynamics in the ARPES of Bi-based TIs are governed by photodissociation or ionization at short time scales, by molecular adsorption at time scales between a very few minutes and the saturation of downward band bending, and by photostimulated desorption and SPV at later times. It is the ensemble of these processes—all of which are inherent to an ARPES experiment conducted at low temperature—that is the reason for the discrepancies

seen between ARPES and magnetotransport experiments as regards the electronic band structure of Bi-based 3D TIs.

#### IV. CONCLUSIONS

Firstly, at a fundamental level, we propose and discuss a sequence of processes that lie behind the complex evolution of the electronic band structure of Bi-based 3D TIs under intense (E)UV illumination. The interplay of molecular adsorption, photodissociation, ionization, photostimulated adsorption, and surface photovoltage are able to account for the observed changes during a typical experiment carried out by means of photon-based techniques such as ARPES. The dynamics of these underlying processes differ significantly, and hence govern the band structure evolution at different time scales.

Secondly, at a practical level, we underline all parameters that need to be taken into account so as to predict the details of the band structure during an ARPES experiment on Bi-based TIs. Most notably, we determine two alternatives in order to approach flat-band conditions with ARPES: measurements after very short or very long illumination times.

Furthermore, we clear up the apparent discrepancies as regards the energy position of the Dirac point from ARPES and SdH oscillations. Therefore, with a view towards possible technological applications based on TIs, our results will facilitate the choice of the most suitable compound.

Last but not least, the established local character of the initial photoinduced changes permits the selection of sample areas where downward band bending is induced. In other words, one may define channels of a combined trivial and topological conduction within a purely topological matrix (by phototriggering the band bending), as a twin to the erasure of the trivial states from the combined system via photostimulated desorption or via surface photovoltage. Such effects might find applications in emerging devices based on topological transport.

#### V. METHODS

##### A. Sample growth

Crystals are grown in Amsterdam using the Bridgman technique. High-purity elements are melted in evacuated, sealed quartz tubes at 850 °C and allowed to mix for 24 h before cooling. The cooling rate is 3 °C per h. Samples are cleaved and aged in UHV ( $P < 5.0 \times 10^{-10}$  mbar) and at temperatures ranging from 16 to 38 K.

##### B. Angle-resolved photoelectron spectroscopy measurements

ARPES experiments are performed at two different experimental setups. (i) At the SIS-HRPES end station of the Swiss Light Source with a Scienta R4000 hemispherical electron analyzer. The minimum temperature is

16 K and the pressure during measurements is  $5.0 \times 10^{-11}$  mbar. (ii) At the UE112-PGM-2a-1<sup>2</sup> end station of BESSY II with a Scienta R8000 hemispherical electron analyzer. The minimum temperature is 38 K and the pressure during measurements is  $1.5 \times 10^{-10}$  mbar.

ARPES data are measured using 27 eV photons (or 30 eV for Bi<sub>2</sub>Se<sub>3</sub>). The polarization is linear horizontal except for data presented in Fig. 4 where we use circular polarization. To determine the effect of photon flux, the latter is deliberately decreased by detuning the undulator energy, while the nominal monochromator energy remains fixed. Relative values of the photon flux are deduced by comparing the ARPES intensity under the same experimental conditions. The duration of each ARPES measurement during the initial evolution of surface band bending is between 1 and 6 s. An accurate determination of the position of the Fermi level is determined from measurements on an *in situ* evaporated Au thin film held in electrical contact with the sample.

#### ACKNOWLEDGMENTS

This work is funded as part of the Foundation for Fundamental Research on Matter (FOM), program 134 on Topological Insulators. FOM is part of the Netherlands Organization for Scientific Research (NWO).

#### APPENDIX: MODEL OF THE MICROSCOPIC MECHANISMS

Here, we use model equations to arrive at a quantitative understanding of the phenomena described in the main text. Using simple formulas, we simulate the microscopic processes of molecular adsorption, photoinduced dissociation and ionization, and photostimulated desorption. Finally, we combine the effects of those processes on the energy shift of the surface electronic structure to arrive at a quantitative description of the evolution of surface band bending. Figure 4 serves as experimental input to describe the time-dependent band bending observed in the surface electronic band structure of Bi<sub>2</sub>Se<sub>3</sub>.

Following Refs. [39,42,63,64], and the discussion in the frame of Fig. 2 of the main text, we assume that, at flat-band conditions, the Fermi level of Bi<sub>2</sub>Se<sub>3</sub> is pinned at the bottom of the conduction band. On exposure to adsorbates and illumination, *n*-type band bending develops and the binding energy of the Dirac point ( $E_D$ ) increases. The uppermost data point in Fig. 4 serves as an approximation for  $E_D$  at flat-band conditions. The surface carrier density  $N_s$  that corresponds to a Fermi level position at 175 meV above  $E_D$  can be expressed as

$$N_s = \frac{k_F^2}{2\pi} \quad \text{and} \quad E_F = \hbar v_F k_F, \quad (\text{A1})$$

where  $E_F$  denotes the energy difference between the Fermi level and the Dirac point (i.e., 175 meV),  $k_F$  is the Fermi

wave vector,  $v_F$  the Fermi velocity, and  $\hbar$  is Planck's constant. The Fermi velocity of  $\text{Bi}_2\text{Se}_3$  is  $5.3 \times 10^5$  m/s (Fig. 4) and the equations yield an intrinsic surface carrier density of  $4.0 \times 10^{12}$   $\text{cm}^{-2}$  at flat-band conditions. This value is in good agreement with what has been previously reported by Brahlek *et al.* in Ref. [63]. We can calculate the extra charges that lead to band bending by the difference of the surface carrier density at maximum band bending and under flat-band conditions. We assume that panel 6 of Fig. 4 shows the ultimate band bending conditions of  $\text{Bi}_2\text{Se}_3$ , and we repeat the aforementioned procedure to find  $N_s = 1.89 \times 10^{13}$   $\text{cm}^{-2}$ . The maximum density of the adsorbate-induced surface carriers is therefore equal to  $1.49 \times 10^{13}$   $\text{cm}^{-2}$ . This density corresponds to 1 charge per  $6.71$   $\text{nm}^2$  and to a coverage of 0.022 adsorbate molecules per substrate atom, under the assumption that we have a single charge per adsorbate and after taking into account the in-plane lattice parameter of  $\text{Bi}_2\text{Se}_3$ .

### 1. Dynamics of molecular adsorption

At low coverages the sticking coefficient ( $s$ ) can be considered constant. The time dependence of the molecular coverage is then given by a simple linear equation:

$$\Theta_{\text{mol}}(t) = sZt, \quad (\text{A2})$$

where  $Z$ , the arrival rate of molecules (collision flux), is given by

$$Z(\text{cm}^{-2} \text{s}^{-1}) = 2.63 \times 10^{22} \frac{P}{\sqrt{MT}}, \quad (\text{A3})$$

with  $P$  denoting the pressure (mbar),  $T$  the temperature (K), and  $M$  the molecular mass (g/mol). Using the values of  $P$  ( $1.5 \times 10^{-10}$  mbar) and  $T$  (38 K) from the caption of Fig. 4, an average molecular mass of 29 g/mol for air molecules, and the surface density of substrate atoms, we can rewrite Eq. (A2) in terms of molecular coverage per substrate atom:

$$\Theta_{\text{mol}}(t) = 1.77 \times 10^{-4} st. \quad (\text{A4})$$

For  $s = 1$ , we need 124 s to obtain a molecular coverage that corresponds to the maximum charge coverage of 0.022. Although there is no previous reference on the sticking probability of air molecules on  $\text{Bi}_2\text{Se}_3$ , the sticking coefficient of the most important contaminant in UHV, molecular hydrogen, has been reported to be much smaller than unity on several different surfaces [66–69]. In order to get an experimental estimate of the sticking probability from the data presented in Fig. 4, we compare the binding energy of the Dirac point in panels 5 and 6, i.e., before and after 90 min in the dark. The molecules that arrive in the surface during this time period are later activated by the light beam and drive the Fermi level 65 meV higher. The corresponding increase in surface density of

adsorbate-induced carriers is equal to  $5.9 \times 10^{12}$   $\text{cm}^{-2}$ . A constant adsorption rate would mean that the coverage of 0.022 adsorbate molecules per substrate atom would be reached in 225 min. A comparison of this value with the value of 124 s obtained assuming a sticking coefficient of unity yields a sticking coefficient  $s$  of the order of 0.01. This result is within the range of the sticking coefficient of molecular hydrogen in the aforementioned past studies [66–69].

The corresponding time-dependent density of adsorbed molecules can be expressed as

$$N_{\text{mol}}(t) = 1.19 \times 10^{15} st, \quad (\text{A5})$$

where the value corresponding to the maximum charge density of  $1.49 \times 10^{13}$   $\text{cm}^{-2} = 1.49 \times 10^{17}$   $\text{m}^{-2}$  is reached in 124 s for  $s = 1$ .

We underline that the maximum charge coverage of 0.022 does not mean that molecular coverage saturates at this value. Charges are continuously being created by photoinduced dissociation and ionization while they are at the same time destroyed by photostimulated desorption. In order to achieve a maximum charge coverage of 0.022, one needs to take into account the charges lost due to desorption and this is only possible if the supply of molecules does not saturate at 0.022 but at a higher value. We denote this last value as  $\Theta_{\text{mol max}}$  and we use it as a partially free parameter in our model with a lower limit of 0.022.

### 2. Dynamics of photoinduced dissociation and ionization

We assume that adsorbed molecules do not yield any charges before their activation with the incoming photons either via photoinduced dissociation (photolysis) or photoionization. We further assume that the dynamics of these processes are identical and they are determined by the absorption of photons. The first step is to calculate the absorption rate of photons ( $R$ ).

$$R = F\sigma_a, \quad (\text{A6})$$

where  $F$  is the photon flux in number of photons/( $\text{s m}^2$ ) and  $\sigma_a$  is the cross section for photon absorption. In the following, we use the photoabsorption cross section of molecular hydrogen at 30 eV ( $\sigma_a = 2.6 \times 10^{-22}$   $\text{m}^2$ ) and we consider the photon flux as a partially free parameter in our model. The upper limit of the photon flux is  $3.2 \times 10^{21}$  photons/( $\text{s m}^2$ ) (flux used in Figs. 1–3 and 5), but we note that the flux used in Fig. 4 is unknown but considerably lower.

Using Eq. (A5), we can now express the rate of absorption events ( $r$ ) as

$$\begin{aligned}
r &= R\Theta_{\text{mol}}(t) = F\sigma_a\Theta_{\text{mol}}(t) \\
&= F(2.6 \times 10^{-22} \times 1.77 \times 10^{-4})st \\
&= Fs(4.6 \times 10^{-26})t,
\end{aligned} \tag{A7}$$

where  $r$  is expressed in number of absorption events/s,  $s$  is the sticking coefficient of the order of 0.01, and  $F$  is the photon flux with an upper limit of  $3.2 \times 10^{21}$  photons/(s m<sup>2</sup>).

We simulate photolysis and photoionization as an exponential process with  $r$  giving the rate constant. The density of the created charges and the corresponding charge coverage can be written as

$$N_{\text{charge creation}}(t) = N_{\text{mol}}(t)(1 - e^{-rt}), \tag{A8}$$

$$\Theta_{\text{charge creation}}(t) = \Theta_{\text{mol}}(t)(1 - e^{-rt}). \tag{A9}$$

$N_{\text{charge creation}}$  and  $\Theta_{\text{charge creation}}$  are limited by the molecular adsorption and, thus, they can never exceed the corresponding values of  $N_{\text{mol}}$  and  $\Theta_{\text{mol}}$ . They will, however, reach values much higher than the calculated maximum values of  $\Theta_{\text{charge tot}} = 0.022$  and  $N_{\text{charge tot}} = 1.49 \times 10^{17}$  m<sup>-2</sup> as charge losses due to photostimulated desorption and surface photovoltage (SPV) are not taken yet into account.

### 3. Dynamics of photostimulated desorption

Here, we model the desorption of surface gas molecules due to the absorption of incoming photons. The removal of these molecules before being activated by photons through photolysis and photoionization means that they cannot yield surface carriers. The process of surface photovoltage that may also result in charge loss is not considered in the following dynamics. The rate of absorption events has already been presented in Eq. (A7). If we assume a first-order desorption process, the time-dependent removal of molecules, in terms of molecular density and coverage, is given by simple exponentials:

$$N_{\text{mol loss}}(t) = N_{\text{mol}}(t)e^{-rt}, \tag{A10}$$

$$\Theta_{\text{mol loss}}(t) = \Theta_{\text{mol}}(t)e^{-rt}, \tag{A11}$$

where those expressions start from a maximum value of molecular density and coverage for  $t = 0$  and tend exponentially towards zero carriers as time increases. These equations take into account the process of molecular adsorption, but they do not consider charge creation via photolysis and photoionization.

### 4. Total dynamics

The challenge now is to combine the dynamics expressed in Eqs. (A8)–(A11) into a single formula that takes into account both the creation and loss of

charges. For the sake of simplicity, we further assume that photostimulated desorption applies only to molecules that have already been activated via photolysis or photoionization. In other words, the first photoabsorption event by an adsorbed molecule always results in its activation via photolysis or ionization: a molecule can be desorbed only after it has been dissociated or ionized. Under this assumption, we can express the total dynamics as follows:

$$N_{\text{charge tot}}(t) = N_{\text{charge creation}}(t)e^{-rt}, \tag{A12}$$

$$\Theta_{\text{charge tot}}(t) = \Theta_{\text{charge creation}}(t)e^{-rt}. \tag{A13}$$

One can readily see that charge loss is now ultimately connected to charge creation, which in turns depends on molecular adsorption via Eqs. (A8) and (A9).

The final time dependence of the Fermi level energy can be calculated using Eq. (A1), where the carrier density is given from Eq. (A12):

$$E_F(t) = \sqrt{2\pi[N_{\text{charge tot}}(t) + 4.0 \times 10^{16}]} \hbar v_F. \tag{A14}$$

We note that the intrinsic charges, already introduced in Appendix A 1, have to be added to the adsorbate-induced charges for the calculation of the Fermi level energy. We recall that the intrinsic carrier density is equal to  $4.0 \times 10^{16}$  m<sup>-2</sup>.

Before plotting the model results, we make two final modifications in the time-dependent equations that describe molecular adsorption [Eqs. (A4) and (A5)]. First of all, molecular adsorption starts already during the time “in the dark.” Therefore, if  $t = 0$  marks the beginning of illumination, Eqs. (A4) and (A5) should become

$$\Theta_{\text{mol}}(t) = 1.77 \times 10^{-4}s(t + t_d), \tag{A15}$$

$$N_{\text{mol}}(t) = 1.19 \times 10^{15}s(t + t_d), \tag{A16}$$

where  $t_d$  denotes the time interval (in seconds) before the first photons arrive on the specific sample location. In the data of Fig. 4,  $t_d$  is of the order of 1.5–2 h for panel 4 and of 3–3.5 h for panel 6.

The last modification is related to a saturation coverage of the adsorbed molecules. Equations (A15) and (A16) describe a molecular coverage and density that increase without a limit. This is physically unreasonable. We therefore make the assumption that both  $\Theta_{\text{mol}}(t)$  and  $N_{\text{mol}}(t)$  reach a plateau at  $\Theta_{\text{mol max}}$  and  $N_{\text{mol max}}$ . These values are considered as a partially free parameter in our model with a lower limit at 0.022 for  $\Theta_{\text{mol max}}$  and at  $1.49 \times 10^{13}$  cm<sup>-2</sup> for  $N_{\text{mol max}}$ . Provided that  $t_d$  is of the order of several minutes or larger (typical for an ARPES experiment), the exact values of the saturation coverage and saturation density modify only slightly the time-dependent quantities expressed by Eqs. (A12)–(A14).

### 5. Model results

The upper panel of Fig. 6 shows the time-dependent coverage (left-hand axis) and density (right-hand axis) of adsorbed molecules and created charges. The black line corresponds to the coverage or density of adsorbed molecules [Eqs. (A15) and (A16)]. The red curve follows the coverage and density of charge carriers created by photolysis and photoionization [Eqs. (A8) and (A9)]. In other words, it shows how many of the adsorbed molecules become “activated” by the photon beam. The green curve denotes the decreasing molecular coverage or density due to photostimulated desorption [Eqs. (A10) and (A11)]. Finally, the blue curve shows the total dynamics: the time-dependent coverage or density of the total charge carriers when we consider charge creation and charge removal as photoinduced sequential events at a specific molecular site [Eqs. (A12) and (A13)]. Best agreement with the experiment is obtained for  $t_d = 8600$  s, a sticking coefficient  $s$  of 0.019, a photon flux  $F$  of  $0.8 \times 10^{20}$  photons/( $s\text{ m}^2$ ), while the values for  $N_{\text{mol max}}$  and  $\Theta_{\text{mol max}}$  have been set to  $4.4 \times 10^{17} \text{ m}^{-2}$  and 0.065. These parameter values are in reasonable agreement with the experimental expectations:  $t_d$  is within the range of 1.5–3.5 h discussed in the previous section, the sticking coefficient is not far from the approximate value of 0.01 calculated from the data of Fig. 4, the photon flux is well below the upper limit of  $3.2 \times 10^{21}$  photons/( $s\text{ m}^2$ ), and the values for  $N_{\text{mol max}}$  and  $\Theta_{\text{mol max}}$  are above the lower limits of  $1.49 \times 10^{17} \text{ m}^{-2}$  and 0.022, respectively. We note that the curves denoting the density and coverage of adsorbed molecules do not start from zero. A large number of molecules have already been adsorbed on the surface before the beginning of illumination. In these conditions, molecular adsorption reaches the saturation values within 20 min. The graph shows that the number of adsorbed molecules is the upper limit of the charges created by photodissociation and ionization. The last processes determine the total charge and total coverage when  $t < 5$  min. At later times the number of activated molecules increases, photostimulated desorption comes into play, and it finally becomes the dominant process when  $t > 15$  min.

The center panel of Fig. 6 follows the complete time dependence of the simulated Fermi level position with respect to  $E_D$  [blue line, Eq. (A14)] using the total density of charge carriers that is shown in the top panel. Moreover, the center panel illustrates the time-dependent Fermi level position due to the charge creation processes of photolysis and photoionization (green curve) and due to the photostimulated desorption (red curve). The red curve has been calculated with  $N_{\text{charge creation}}(t)$  as input for the time-dependent carrier density, in other words, as if a desorption process was not taking place. On the other hand, the green curve has been calculated with  $N_{\text{mol loss}}(t)$  as input for the time-dependent carrier density, in other words, as if each molecule gave rise to a charge carrier before being desorbed and as if photolysis and photoionization were not taking place. As expected, the complete time

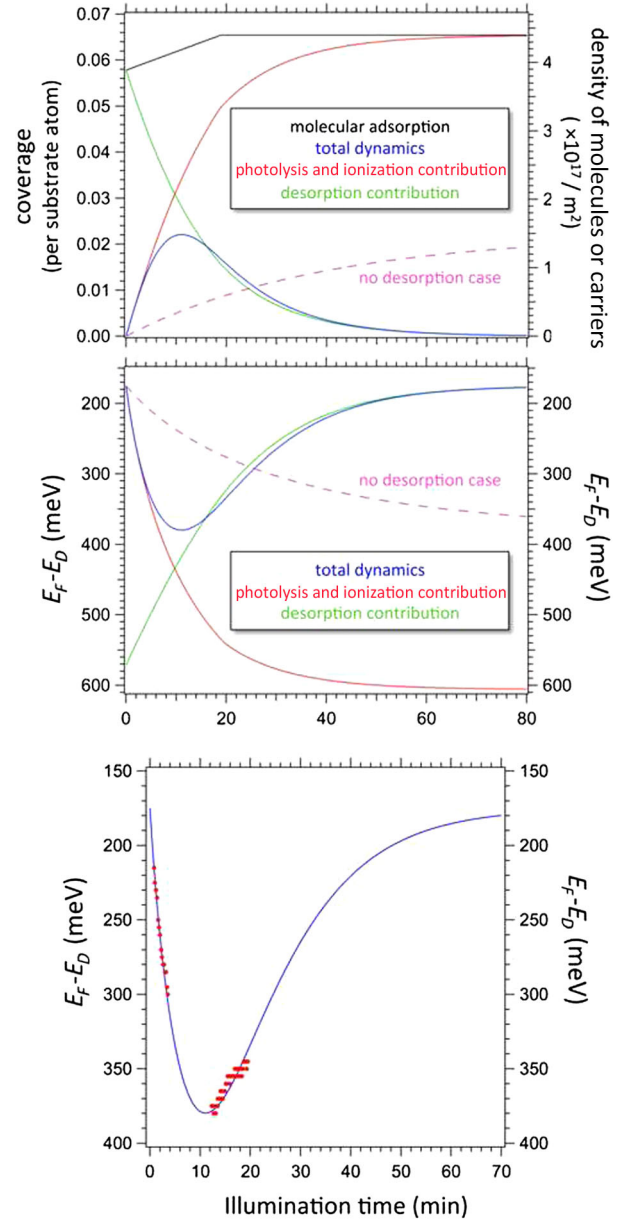


FIG. 6. A quantitative model of the microscopic procedures behind the surface band bending in 3D TIs. Top: Time-dependent coverage or density of adsorbed molecules and created charges. Black, red, and green curves follow the coverage or density of, respectively, adsorbed molecules, charges created by photoinduced processes, and molecules desorbed due to incoming photons. Center: Corresponding time-dependent energy value of the Fermi level with respect to the Dirac point. Red and green curves follow the energy variation due to photoinduced processes of charge creation and molecular desorption, respectively. In both the top and center panels, the blue curve shows the total dynamics under the assumption that photostimulated desorption at a local site occurs only after the “activation” of the specific molecule. The dashed curve describes the total dynamics if in the absence of photostimulated desorption the maximum value of surface band bending were to stay unaltered. Bottom: Time-dependent energy variation of the Fermi level in comparison with the experimental data of Fig. 4 showing that the down-shift and up-shift rates are well reproduced. Details on the model parameters are given in the text.

dependence of the Fermi level position is determined by photolysis and photoionization at early times and by photo-stimulated desorption at later times. The dashed curves denote the time-dependent carrier density and coverage to reach the Fermi level position corresponding to maximum band bending in the absence of desorption. In that case, the maximum coverage and carrier density reach the values calculated in the first part of the Appendix (i.e., 0.022 and  $1.49 \times 10^{13} \text{ cm}^{-2}$ , respectively). Finally, the bottom panel of Fig. 6 compares the time dependence of the Fermi level position with respect to  $E_D$  with the experimental data points of Fig. 4. We note that the rates of both the down-shift (data points from location C) and the up-shift (data points from location D) are very well reproduced.

Figure 7 shows the predictability of our model. The top panel compares the time dependence of the Fermi level position for different values of the incoming photon flux.

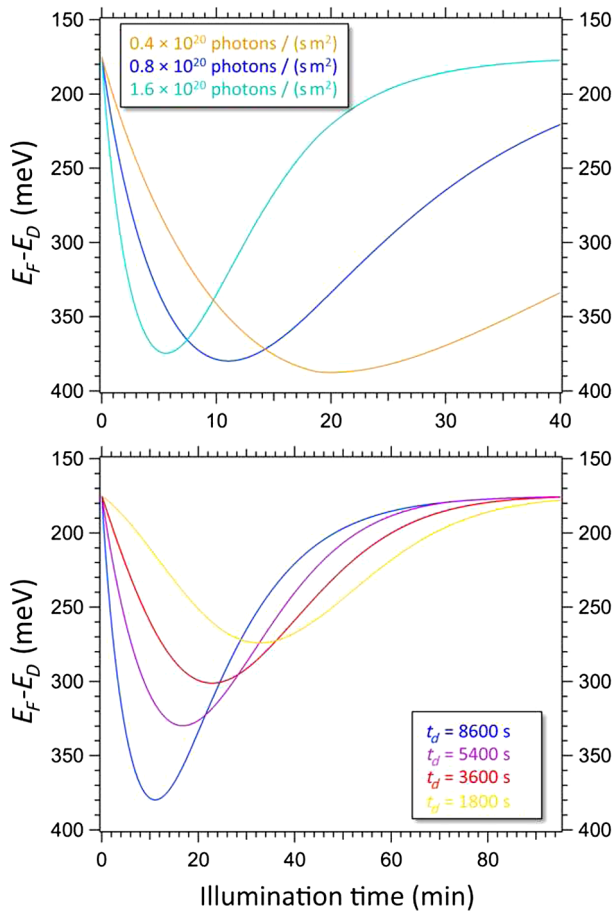


FIG. 7. The simulated effect of photon flux and surface decoration on the surface band bending in 3D TIs. Top: Time-dependent energy value of the Fermi level with respect to the Dirac point for various values of the incoming photon flux. Bottom: Time-dependent energy value of the Fermi level with respect to the Dirac point for various time intervals of the surface decoration while the sample was still in the dark. All other parameters of the model are described in the text and they are identical to those used in Fig. 6.

The original value of  $F = 0.8 \times 10^{20} \text{ photons}/(\text{s m}^2)$  yields the blue curve, while the cyan and orange curves correspond to values of  $2F$  and  $F/2$ , respectively. The time evolution of the energy shifts becomes faster with increasing photon flux, as experimentally confirmed in Fig. 4. We note that increasing photon energy could theoretically have the opposite effect from increasing photon flux. This is because the photoabsorption cross section can strongly decrease when  $h\nu$  is higher, giving rise to a smaller rate of absorption events [Eq. (A7)]. In practice, the effect of increasing  $h\nu$  is more complex. As we have previously discussed in Ref. [39], increasing  $h\nu$  boosts the surface photovoltage process leading to a more effective band flattening through the creation of a larger number of electron-hole pairs.

The bottom panel of Fig. 7 simulates the effect of surface decoration before the first illumination. The blue curve is the original simulation obtained for  $t_d = 8600 \text{ s}$  (2.4 h). The other curves show the time evolution of the Fermi level when  $t_d$  changes to 1.5 h (purple), 1 h (red), and 0.5 h (yellow). As time in the dark decreases, the time evolution becomes slower and the total energy shift becomes smaller. These effects are in good agreement with the experimental results presented in Fig. 3. A smaller time in the dark translates into fewer adsorbed molecules at early times and hence into fewer charges from photolysis and photoionization before desorption sets in.

The described model of molecular adsorption and photo-stimulated processes can simulate our experimental data in a satisfactory way, and it can, moreover, correctly predict the system's behavior when certain external parameters are modified. Because of its simplicity, shortcomings are not surprising. As an example, we note the underestimation of the time intervals when the Fermi level position barely changes (e.g., Fig. 4, location D). Future improvements require a more refined model that takes into consideration the surface photovoltage process and the possibility of molecular desorption before dissociation or ionization. The inclusion of surface photovoltage in the band flattening process has indeed been the focus of one of our previous studies [39]. Despite the possibility of more sophisticated simulations, we strongly believe that our simple model already includes the essential physics that govern the time dependence of the electronic structure of TIs.

- [1] M. Z. Hasan and C. L. Kane, *Colloquium: Topological Insulators*, *Rev. Mod. Phys.* **82**, 3045 (2010).
- [2] L. Fu and C. L. Kane, *Topological Insulators with Inversion Symmetry*, *Phys. Rev. B* **76**, 045302 (2007).
- [3] Y. Xia, D. Qian, D. Hsieh, L. Wray, A. Pal, H. Lin, A. Bansil, D. Grauer, Y. S. Hor, R. J. Cava, and M. Z. Hasan, *Observation of a Large-Gap Topological-Insulator Class with a Single Dirac Cone on the Surface*, *Nat. Phys.* **5**, 398 (2009).

- [4] Y. L. Chen, J. G. Analytis, J.-H. Chu, Z. K. Liu, S.-K. Mo, X. L. Qi, H. J. Zhang, D. H. Lu, X. Dai, Z. Fang, S. C. Zhang, I. R. Fisher, Z. Hussain, and Z.-X. Shen, *Experimental Realization of a Three-Dimensional Topological Insulator*,  $\text{Bi}_2\text{Te}_3$ , *Science* **325**, 178 (2009).
- [5] H. Zhang, C.-X. Liu, X.-L. Qi, X. Dai, Z. Fang, and S.-C. Zhang, *Topological Insulators in  $\text{Bi}_2\text{Se}_3$ ,  $\text{Bi}_2\text{Te}_3$  and  $\text{Sb}_2\text{Te}_3$  with a Single Dirac Cone on the Surface*, *Nat. Phys.* **5**, 438 (2009).
- [6] Y. L. Chen, Z. K. Liu, J. G. Analytis, J.-H. Chu, H. J. Zhang, B. H. Yan, S.-K. Mo, R. G. Moore, D. H. Lu, I. R. Fisher, S. C. Zhang, Z. Hussain, and Z.-X. Shen, *Single Dirac Cone Topological Surface State and Unusual Thermoelectric Property of Compounds from a New Topological Insulator Family*, *Phys. Rev. Lett.* **105**, 266401 (2010).
- [7] M. Bianchi, D. Guan, S. Bao, J. Mi, B. B. Iversen, P. D. C. King, and Ph. Hofmann, *Coexistence of the Topological State and a Two-Dimensional Electron Gas on the Surface of  $\text{Bi}_2\text{Se}_3$* , *Nat. Commun.* **1**, 128 (2010).
- [8] P. D. C. King *et al.*, *Large Tunable Rashba Spin Splitting of a Two-Dimensional Electron Gas in  $\text{Bi}_2\text{Se}_3$* , *Phys. Rev. Lett.* **107**, 096802 (2011).
- [9] L. Fu, *Topological Crystalline Insulators*, *Phys. Rev. Lett.* **106**, 106802 (2011).
- [10] Y. Tanaka, Z. Ren, T. Sato, K. Nakayama, S. Souma, T. Takahashi, K. Segawa, and Y. Ando, *Experimental Realization of a Topological Crystalline Insulator in  $\text{SnTe}$* , *Nat. Phys.* **8**, 800 (2012).
- [11] P. Dziawa, B. J. Kowalski, K. Dybko, R. Buczko, A. Szczerbakow, M. Szot, E. Łusakowska, T. Balasubramanian, B. M. Wojek, M. H. Bernstena, O. Tjernberg, and T. Story, *Topological Crystalline Insulator States in  $\text{Pb}_{1-x}\text{Sn}_x\text{Se}$* , *Nat. Mater.* **11**, 1023 (2012).
- [12] R.-J. Slager, A. Mesaros, V. Juričić, and J. Zaanen, *The Space Group Classification of Topological Band-Insulators*, *Nat. Phys.* **9**, 98 (2013).
- [13] Z. K. Liu, B. Zhou, Y. Zhang, Z. J. Wang, H. M. Weng, D. Prabhakaran, S.-K. Mo, Z. X. Shen, Z. Fang, X. Dai, Z. Hussain, and Y. L. Chen, *Discovery of a Three-Dimensional Topological Dirac Semimetal,  $\text{Na}_3\text{Bi}$* , *Science* **343**, 864 (2014).
- [14] M. Neupane, S.-Y. Xu, R. Sankar, N. Alidoust, G. Bian, C. Liu, I. Belopolski, T.-R. Chang, H.-T. Jeng, H. Lin, A. Bansil, F. Chou, and M. Z. Hasan, *Observation of a Three-Dimensional Topological Dirac Semimetal Phase in High-Mobility  $\text{Cd}_3\text{As}_2$* , *Nat. Commun.* **5**, 3786 (2014).
- [15] S.-Y. Xu, I. Belopolski, N. Alidoust, M. Neupane, G. Bian, C. Zhang, R. Sankar, G. Chang, Z. Yuan, C.-C. Lee, S.-M. Huang, H. Zheng, J. Ma, D. S. Sanchez, B. Wang, A. Bansil, F. Chou, P. P. Shibayev, H. Lin, S. Jian, and M. Z. Hasan, *Discovery of a Weyl Fermion Semimetal and Topological Fermi Arcs*, *Science* **349**, 613 (2015).
- [16] D. Hsieh, Y. Xia, D. Qian, L. Wray, J. H. Dil, F. Meier, J. Osterwalder, L. Patthey, J. G. Checkelsky, N. P. Ong, A. V. Fedorov, H. Lin, A. Bansil, D. Grauer, Y. S. Hor, R. J. Cava, and M. Z. Hasan, *A Tunable Topological Insulator in the Spin Helical Dirac Transport Regime*, *Nature (London)* **460**, 1101 (2009).
- [17] A. Stern and N. H. Lindner, *Topological Quantum Computation—From Basic Concepts to First Experiments*, *Science* **339**, 1179 (2013).
- [18] S. M. Albrecht, A. P. Higginbotham, M. Madsen, F. Kuemmeth, T. S. Jespersen, J. Nygård, P. Krogstrup, and C. M. Marcus, *Exponential Protection of Zero Modes in Majorana Islands*, *Nature (London)* **531**, 206 (2016).
- [19] V. Mourik, K. Zuo, S. M. Frolov, S. R. Plissard, E. P. A. M. Bakkers, and L. P. Kouwenhoven, *Signatures of Majorana Fermions in Hybrid Superconductor-Semiconductor Nanowire Devices*, *Science* **339**, 1179 (2013).
- [20] M. Bianchi, R. C. Hatch, J. Mi, B. B. Iversen, and Ph. Hofmann, *Simultaneous Quantization of Bulk Conduction and Valence States through Adsorption of Nonmagnetic Impurities on  $\text{Bi}_2\text{Se}_3$* , *Phys. Rev. Lett.* **107**, 086802 (2011).
- [21] H. M. Benia, C. Lin, K. Kern, and C. R. Ast, *Reactive Chemical Doping of the  $\text{Bi}_2\text{Se}_3$  Topological Insulator*, *Phys. Rev. Lett.* **107**, 177602 (2011).
- [22] Z.-H. Zhu, G. Levy, B. Ludbrook, C. N. Veenstra, J. A. Rosen, R. Comin, D. Wong, P. Dosanjh, A. Ubaldini, P. Syers, N. P. Butch, J. Paglione, I. S. Elfimov, and A. Damascelli, *Rashba Spin-Splitting Control at the Surface of the Topological Insulator  $\text{Bi}_2\text{Se}_3$* , *Phys. Rev. Lett.* **107**, 186405 (2011).
- [23] M. S. Bahramy, P. D. C. King, A. de la Torre, J. Chang, M. Shi, L. Patthey, G. Balakrishnan, Ph. Hofmann, R. Arita, N. Nagaosa, and F. Baumberger, *Emergent Quantum Confinement at Topological Insulator Surfaces*, *Nat. Commun.* **3**, 1159 (2012).
- [24] C. Chen, S. He, H. Weng, W. Zhang, L. Zhao, H. Liu, X. Jia, D. Mou, S. Liu, J. He, Y. Peng, Y. Feng, Z. Xie, G. Liu, X. Dong, J. Zhang, X. Wang, Q. Peng, Z. Wang, S. Zhang, F. Yang, C. Chen, Z. Xu, X. Dai, Z. Fang, and X. J. Zhou, *Robustness of Topological Order and Formation of Quantum Well States in Topological Insulators Exposed to Ambient Environment*, *Proc. Natl. Acad. Sci. U.S.A.* **109**, 3694 (2012).
- [25] M. Bianchi, R. C. Hatch, Z. Li, Ph. Hofmann, F. Song, J. Mi, B. B. Iversen, Z. M. Abd El-Fattah, P. Löptien, L. Zhou, A. A. Khajetoorians, J. Wiebe, R. Wiesendanger, and J. W. Wells, *Robust Surface Doping of  $\text{Bi}_2\text{Se}_3$  by Rubidium Intercalation*, *ACS Nano* **6**, 7009 (2012).
- [26] T. Valla, Z.-H. Pan, D. Gardner, Y. S. Lee, and S. Chu, *Photoemission Spectroscopy of Magnetic and Nonmagnetic Impurities on the Surface of the  $\text{Bi}_2\text{Se}_3$  Topological Insulator*, *Phys. Rev. Lett.* **108**, 117601 (2012).
- [27] B. Zhou, Z. K. Liu, J. G. Analytis, K. Igarashi, S. K. Mo, D. H. Lu, R. G. Moore, I. R. Fisher, T. Sasagawa, and Z. X. Shen, *Controlling the Carriers of Topological Insulators by Bulk and Surface Doping*, *Semicond. Sci. Technol.* **27**, 124002 (2012).
- [28] M. R. Scholz, J. Sánchez-Barriga, D. Marchenko, A. Varykhalov, A. Volykhov, L. V. Yashina, and O. Rader, *Tolerance of Topological Surface States towards Magnetic Moments: Fe on  $\text{Bi}_2\text{Se}_3$* , *Phys. Rev. Lett.* **108**, 256810 (2012).
- [29] N. de Jong, E. Frantzeskakis, B. Zwartsenberg, Y. K. Huang, D. Wu, P. Hlawenka, J. Sánchez-Barriga, A. Varykhalov, E. van Heumen, and M. S. Golden, *Angle-Resolved and Core-Level Photoemission Study of Interfacial the Topological Insulator  $\text{Bi}_{1.5}\text{Sb}_{0.5}\text{Te}_{1.7}\text{Se}_{1.3}$  with Ag, Nb, and Fe*, *Phys. Rev. B* **92**, 075127 (2015).
- [30] S. Jia, H. Ji, E. Climent-Pascual, M. K. Fuccillo, M. E. Charles, J. Xiong, N. P. Ong, and R. J. Cava,

- Low-Carrier-Concentration Crystals of the Topological Insulator Bi<sub>2</sub>Te<sub>2</sub>Se*, *Phys. Rev. B* **84**, 235206 (2011).
- [31] Z. Ren, A. A. Taskin, S. Sasaki, K. Segawa, and Y. Ando, *Large Bulk Resistivity and Surface Quantum Oscillations in the Topological Insulator Bi<sub>2</sub>Te<sub>2</sub>Se*, *Phys. Rev. B* **82**, 241306 (2010).
- [32] T. Arakane, T. Sato, S. Souma, K. Kosaka, K. Nakayama, M. Komatsu, T. Takahashi, Z. Ren, Kouji Segawa, and Y. Ando, *Tunable Dirac Cone in the Topological Insulator Bi<sub>2-x</sub>Sb<sub>x</sub>Te<sub>3-y</sub>Se<sub>y</sub>*, *Nat. Commun.* **3**, 636 (2012).
- [33] M. Neupane, S.-Y. Xu, L. A. Wray, A. Petersen, R. Shankar, N. Alidoust, C. Liu, A. Fedorov, H. Ji, J. M. Allred, Y. S. Hor, T.-R. Chang, H.-T. Jeng, H. Lin, A. Bansil, R. J. Cava, and M. Z. Hasan, *Topological Surface States and Dirac Point Tuning in Ternary Topological Insulators*, *Phys. Rev. B* **85**, 235406 (2012).
- [34] K. Miyamoto, A. Kimura, T. Okuda, H. Miyahara, K. Kuroda, H. Namatame, M. Taniguchi, S. V. Eremeev, T. V. Menshchikova, E. V. Chulkov, K. A. Kokh, and O. E. Tereshchenko, *Topological Surface States with Persistent High Spin Polarization across the Dirac Point in Bi<sub>2</sub>Te<sub>2</sub>Se and Bi<sub>2</sub>Se<sub>2</sub>Te*, *Phys. Rev. Lett.* **109**, 166802 (2012).
- [35] Y. Pan, D. Wu, J. R. Angevaere, H. Luigjes, E. Frantzeskakis, N. de Jong, E. van Heumen, T. V. Bay, B. Zwartsenberg, Y. K. Huang, M. Snelder, A. Brinkman, M. S. Golden, and A. de Visser, *Low Carrier Concentration Crystals of the Topological Insulator Bi<sub>2-x</sub>Sb<sub>x</sub>Te<sub>3-y</sub>Se<sub>y</sub>: A Magnetotransport Study*, *New J. Phys.* **16**, 123035 (2014).
- [36] Y. Pan, A. M. Nikitin, D. Wu, Y. K. Huang, A. Puri, S. Wiedmann, U. Zeitler, E. Frantzeskakis, E. van Heumen, M. S. Golden, and A. de Visser, *Quantum Oscillations of the Topological Surface States in Low Carrier Concentration Crystals of Bi<sub>2-x</sub>Sb<sub>x</sub>Te<sub>3-y</sub>Se<sub>y</sub>*, *Solid State Commun.* **227**, 13 (2016).
- [37] A. A. Kordyuk, T. K. Kim, V. B. Zabolotnyy, D. V. Evtushinsky, M. Bauch, C. Hess, B. Büchner, H. Berger, and S. V. Borisenko, *Photoemission-Induced Gating of Topological Insulators*, *Phys. Rev. B* **83**, 081303 (2011).
- [38] R. Jiang, L.-L. Wang, M. Huang, R. S. Dhaka, D. D. Johnson, T. A. Lograsso, and A. Kaminski, *Reversible Tuning of the Surface State in a Pseudobinary Bi<sub>2</sub>(Te-Se)<sub>3</sub> Topological Insulator*, *Phys. Rev. B* **86**, 085112 (2012).
- [39] E. Frantzeskakis *et al.*, *Dirac States with Knobs On: Interplay of External Parameters and the Surface Electronic Properties of Three-Dimensional Topological Insulators*, *Phys. Rev. B* **91**, 205134 (2015).
- [40] L. A. Wray, S.-Y. Xu, Y. Xia, D. Hsieh, A. V. Fedorov, Y. S. Hor, R. J. Cava, A. Bansil, H. Lin, and M. Z. Hasan, *A Topological Insulator Surface under Strong Coulomb, Magnetic and Disorder perturbations*, *Nat. Phys.* **7**, 32 (2011).
- [41] M. Petrushevsky, E. Lahoud, A. Ron, E. Maniv, I. Diamant, I. Neder, S. Wiedmann, V. K. Guduru, F. Chiappini, U. Zeitler, J. C. Maan, K. Chashka, A. Kanigel, and Y. Dagan, *Probing the Surface States in Bi<sub>2</sub>Se<sub>3</sub> Using the Shubnikov-de Haas Effect*, *Phys. Rev. B* **86**, 045131 (2012).
- [42] J. G. Analytis, J.-H. Chu, Y. Chen, F. Corredor, R. D. McDonald, Z. X. Shen, and I. R. Fisher, *Bulk Fermi Surface Coexistence with Dirac Surface State in Bi<sub>2</sub>Se<sub>3</sub>: A Comparison of Photoemission and Shubnikov-de Haas Measurements*, *Phys. Rev. B* **81**, 205407 (2010).
- [43] M. Bianchi, R. C. Hatch, D. Guan, T. Planke, J. Mi, B. B. Iversen, and Ph. Hofmann, *The Electronic Structure of Clean and Adsorbate-Covered Bi<sub>2</sub>Se<sub>3</sub>: An Angle-Resolved Photoemission Study*, *Semicond. Sci. Technol.* **27**, 124001 (2012).
- [44] D. Hsieh, Y. Xia, D. Qian, L. Wray, F. Meier, J. H. Dil, J. Osterwalder, L. Patthey, A. V. Fedorov, H. Lin, A. Bansil, D. Grauer, Y. S. Hor, R. J. Cava, and M. Z. Hasan, *Observation of Time-Reversal-Protected Single-Dirac-Cone Topological-Insulator States in Bi<sub>2</sub>Te<sub>3</sub> and Sb<sub>2</sub>Te<sub>3</sub>*, *Phys. Rev. Lett.* **103**, 146401 (2009).
- [45] H.-J. Noh, H. Koh, S.-J. Oh, J.-H. Park, H.-D. Kim, J. D. Rameau, T. Valla, T. E. Kidd, P. D. Johnson, and Y. Hu, *Spin-Orbit Interaction Effect in the Electronic Structure of Bi<sub>2</sub>Te<sub>3</sub> Observed by Angle-Resolved Photoemission Spectroscopy*, *Europhys. Lett.* **81**, 57006 (2008).
- [46] M. R. Scholz, J. Sánchez-Barriga, J. Braun, D. Marchenko, A. Varykhalov, M. Lindroos, Y. J. Wang, H. Lin, A. Bansil, J. Minár, H. Ebert, A. Volykhov, L. V. Yashina, and O. Rader, *Reversal of the Circular Dichroism in Angle-Resolved Photoemission from Bi<sub>2</sub>Te<sub>3</sub>*, *Phys. Rev. Lett.* **110**, 216801 (2013).
- [47] H. Cao, C. Liu, J. Tian, Y. Xu, I. Miotkowski, M. Z. Hasan, and Y. P. Chen, *Controlling and Distinguishing Electronic Transport of Topological and Trivial Surface States in a Topological Insulator*, *arXiv:1409.3217*.
- [48] L. Bao, L. He, N. Meyer, X. Kou, P. Zhang, Z.-G. Chen, A. V. Fedorov, J. Zhou, T. M. Riedemann, T. A. Lograsso, K. L. Wang, G. Tuttle, and F. Xiu, *Weak Anti-Localization and Quantum Oscillations of Surface States in Topological Insulator Bi<sub>2</sub>Se<sub>2</sub>Te*, *Sci. Rep.* **2**, 726 (2012).
- [49] Y. Yan, L.-X. Wang, X. Ke, G. Van Tendeloo, X.-S. Wu, D.-P. Yu, and Z.-M. Liao, *High-Mobility Bi<sub>2</sub>Se<sub>3</sub> Nanoplates Manifesting Quantum Oscillations of Surface States in the Sidewalls*, *Sci. Rep.* **4**, 3817 (2014).
- [50] A. A. Taskin, S. Sasaki, K. Segawa, and Y. Ando, *Manifestation of Topological Protection in Transport Properties of Epitaxial Bi<sub>2</sub>Se<sub>3</sub> Thin Films*, *Phys. Rev. Lett.* **109**, 066803 (2012).
- [51] A. A. Taskin, S. Sasaki, K. Segawa, and Y. Ando, *Achieving Surface Quantum Oscillations in Topological Insulator Thin Films of Bi<sub>2</sub>Se<sub>3</sub>*, *Adv. Mater.* **24**, 5581 (2012).
- [52] N. Kim, P. Lee, Y. Kim, J. S. Kim, Y. Kim, D. Y. Noh, S. U. Yu, J. Chung, and K. S. Kim, *Persistent Topological Surface State at the Interface of Bi<sub>2</sub>Se<sub>3</sub> Film Grown on Patterned Graphene*, *ACS Nano* **8**, 1154 (2014).
- [53] L. He, F. Xiu, X. Yu, M. Teague, W. Jiang, Y. Fan, X. Kou, M. Lang, Y. Wang, G. Huang, N.-C. Yeh, and K. L. Wang, *Surface-Dominated Conduction in a 6 nm Thick Bi<sub>2</sub>Se<sub>3</sub> Thin Film*, *Nano Lett.* **12**, 1486 (2012).
- [54] J. G. Analytis, R. D. McDonald, S. C. Riggs, J.-H. Chu, G. S. Boebinger, and I. R. Fisher, *Two-Dimensional Surface State in the Quantum Limit of a Topological Insulator*, *Nat. Phys.* **6**, 960 (2010).
- [55] D.-X. Qu, Y. S. Hor, and R. J. Cava, *Quantum Oscillations in Magnetothermopower Measurements of the Topological Insulator Bi<sub>2</sub>Te<sub>3</sub>*, *Phys. Rev. Lett.* **109**, 246602 (2012).

- [56] L. N. Luk'yanova, Y. A. Boikov, V. A. Danilov, O. A. Usov, M. P. Volkov, and V. A. Kutasov, *Surface Morphology and Raman Spectroscopy of Thin Layers of Antimony and Bismuth Chalcogenides*, *Phys. Solid State* **56**, 941 (2014).
- [57] D.-X. Qu, Y. S. Hor, J. Xiong, R. J. Cava, and N. P. Ong, *Quantum Oscillations and Hall Anomaly of Surface States in the Topological Insulator Bi<sub>2</sub>Te<sub>3</sub>*, *Science* **329**, 821 (2010).
- [58] J. Xiong, A. C. Petersen, D. Qu, Y. S. Hor, R. J. Cava, and N. P. Ong, *Quantum Oscillations in a Topological Insulator Bi<sub>2</sub>Te<sub>2</sub>Se with Large Bulk Resistivity (6 Ω cm)*, *Physica (Amsterdam)* **44E**, 917 (2012).
- [59] J. Xiong, Y. Luo, Y. H. Khoo, S. Jia, R. J. Cava, and N. P. Ong, *High-Field Shubnikov–de Haas Oscillations in the Topological Insulator Bi<sub>2</sub>Te<sub>2</sub>Se*, *Phys. Rev. B* **86**, 045314 (2012).
- [60] A. A. Taskin, Z. Ren, S. Sasaki, K. Segawa, and Y. Ando, *Observation of Dirac Holes and Electrons in a Topological Insulator*, *Phys. Rev. Lett.* **107**, 016801 (2011).
- [61] T.-C. Hsiung, D.-Y. Chen, L. Zhao, Y.-H. Lin, C.-Y. Mou, T.-K. Lee, M.-K. Wu, and Y.-Y. Chen, *Enhanced Surface Mobility and Quantum Oscillations in Topological Insulator Bi<sub>1.5</sub>Sb<sub>0.5</sub>Te<sub>1.7</sub>Se<sub>1.3</sub> Nanoflakes*, *Appl. Phys. Lett.* **103**, 163111 (2013).
- [62] E. Frantzeskakis, N. de Jong, B. Zwartsenberg, Y. K. Huang, T. V. Bay, P. Pronk, E. van Heumen, D. Wu, Y. Pan, M. Radovic, N. C. Plumb, N. Xu, M. Shi, A. de Visser, and M. S. Golden, *Micro-Metric Electronic Patterning of a Topological Band Structure Using a Photon Beam*, *Sci. Rep.* **5**, 16309 (2015).
- [63] M. Brahlek, N. Koirala, N. Bansal, and S. Oh, *Transport Properties of Topological Insulators: Band Bending, Bulk Metal-to-Insulator Transition, and Weak Anti-Localization*, *Solid State Commun.* **215–216**, 54 (2015).
- [64] R. J. Cava, H. Ji, M. K. Fuccillo, Q. D. Gibson, and Y. S. Hor, *Crystal Structure and Chemistry of Topological Insulators*, *J. Mater. Chem. C* **1**, 3176 (2013).
- [65] Z. Ren, A. A. Taskin, S. Sasaki, K. Segawa, and Y. Ando, *Optimizing Bi<sub>2-x</sub>Sb<sub>x</sub>Te<sub>3-y</sub>Se<sub>y</sub> Solid Solutions to Approach the Intrinsic Topological Insulator Regime*, *Phys. Rev. B* **84**, 165311 (2011).
- [66] A. Winkler and K. D. Rendulic, *Adsorption Kinetics for Hydrogen Adsorption on Nickel and Coadsorption of Hydrogen and Oxygen*, *Surf. Sci.* **118**, 19 (1982).
- [67] H. F. Berger, Ch. Resch, E. Grösslinger, G. Eilmsteiner, A. Winkler, and K. D. Rendulic, *Adsorption of Hydrogen on Tungsten: A Precursor Path Plus Direct Adsorption*, *Surf. Sci. Lett.* **275**, L627 (1992).
- [68] A. Winkler, *Interaction of Atomic Hydrogen with Metal Surfaces*, *Appl. Phys. A* **67**, 637 (1998).
- [69] P. Kraus, Ch. Gösweiner, A. Tamtögl, F. Apolloner, and W. E. Ernst, *Adhesion Properties of Hydrogen on Sb(111) Probed by Helium Atom Scattering*, *Europhys. Lett.* **114**, 56001 (2016).